Journal of Translational Medicine

RESEARCH

Open Access

TGF-β/JNK axis mediates mitochondrial damage and macrophage cGAS-STING activation in liver Mallory-Denk body pathogenesis

Yi Shi[1,2,5], Maoping Huang[1,5], Wanmei Zhou[1,2,5], Yi Zhao[1,2,5], Jiuying Zhao[1,2,5], Bei Zhong[1,5], Samuel W. French[3], Xiaoping Tang[2,4*] and Hui Liu[1,2,5*]

Abstract

Background Mallory-Denk bodies (MDBs) are characteristic proteins and inflammatory aggregates appeared in drug-induced chronic liver injury and various chronic liver disease. MDBs formation is often accompanied with mitochondrial damage and inflammatory environment. However, how mitochondrial damage and inflammatory response affect the pathological process of MDBs is largely unknown. The scope of this study was to provide unprecedented insights into the mechanism of MDBs pathogenesis and the potential target of transforming growth factor beta (TGF-β)/JNK axis in the treatment of MDB-related chronic liver disease.

Methods Single-nucleus RNA sequencing (snRNA-seq), typical MDB-related multiplex immunofluorescence staining and functional in vitro and in vivo experiments were performed to investigate the potential mechanisms of TGF-β/JNK axis in the process of MDBs formation in chronic liver injury. Furthermore, the TGF-β/JNK axis has been demonstrated to be activated in clinical patients with metabolic dysfunction-associated steatotic liver disease (MASLD), which implies the potential clinical implications of the TGF-β/JNK axis.

Results Our study delineates a hepatocyte-macrophage crosstalk axis wherein TGF-β/TGF-βR dysregulation drives JNK-mediated MDBs pathogenesis. Mechanistically, the activation of JNK pathway upregulates downstream c-JUN expression ($p < 0.0009$, $n = 3$) and directly contributes to MDBs formation by promoting transcriptional activation of UbD. Concurrently, JNK signaling promotes BAX/BAK oligomerization, triggering mitochondrial translocation and subsequent generation of mitochondria-derived vesicles (MDVs), as evidenced by the significantly enhanced colocalization between damaged mtDNA and the mitochondrial outer membrane marker TOM20 in the experimental group compared to controls ($p = 0.0001$, $n = 5$). Then, following transport to macrophages, mtDNA escapes from MDVs, activating the cGAS-STING signaling and subsequently mediating IL-6 pro-inflammatory cytokine release ($p = 0.0006$, $n = 3$). Notably, the inhibition of JNK signaling attenuated both MDBs formation ($p = 0.0027$, $n = 3$) and IL-6 secretion ($p = 0.0658$, $n = 3$), demonstrating therapeutic potential through dual cytoprotective and immunomodulatory effects.

*Correspondence:
Xiaoping Tang
tangxp@gzhmu.edu.cn
Hui Liu
liuhui806@gzhmu.edu.cn
Full list of author information is available at the end of the article

Conclusions This study identifies the novel regulatory mechanism of the TGF-β/JNK signaling axis in MDBs formation, delivering mechanistic insights into MDB-associated chronic liver disease. Inhibition of JNK pathway suppresses MDBs formation while alleviates the inflammatory microenvironment by attenuating mitochondrial damage. Blocking the TGF-β/JNK signaling axis may represent a potential therapeutic strategy for MDB-associated chronic liver disease.

Keywords Inflammation, Mallory-Denk bodies (MDBs), Mitochondrial damage, cGAS-STING signaling, TGF-β/JNK axis

Introduction

Cancer has become a predominant threat to human health in modern society, with environmental factors such as chiral pesticides, pollutants, and pharmaceutical agents emerging as potential carcinogenic contributors [1]. Notably, hepatocellular carcinoma (HCC) maintains persistently high global incidence and mortality rates among malignancies [2]. This urgent scenario demands comprehensive investigation into oncogenic mechanisms, discovery of optimized anticancer therapeutics, and development of innovative treatment paradigms. Recent advancements highlight glutamic acid derivatives as promising anticancer agents, complemented by antifungal pyrazolyl ligand-based therapies utilizing copper (II) and nickel (II) complexes [3–5]. Furthermore, Emerging research separately validates the therapeutic potential of phytotherapeutic approaches and polymeric nanoformulations in oncology treatment paradigms [6, 7]. These innovations collectively present novel strategic approaches for oncology treatment development.

Mallory-Denk bodies (MDBs) are hallmark features of chronic liver diseases, including alcoholic hepatitis [8, 9], metabolic dysfunction-associated steatohepatitis (MASH), cirrhosis, and HCC. They hold significant diagnostic value in these contexts [10]. MDBs formation has been linked to proteasomal misfolding and overload [11]. However, the underlying molecular mechanisms and inflammatory pathways driving their pathogenesis remain poorly understood.

Transforming growth factor-beta (TGF-β) plays a pivotal role in liver disease progression, acting as both a pro-inflammatory and anti-inflammatory mediator [12]. While the canonical SMAD-dependent signaling cascade downstream of TGF-β has been extensively studied [13]. However, emerging evidence suggests non-classical apoptotic pathways may contribute to TGF-β -mediated disease progression. Notably, TGF-β activation of JNK pathway has been implicated in fibrotic remodeling of hepatic and renal tissues [14], though its specific role in modulating inflammatory cascades requires further elucidation.

Mitochondrial homeostasis serves as a critical determinant of hepatic cellular integrity. Beyond their primary role in energy metabolism, mitochondria mediate intracellular signaling networks and respond to pathological stress through the release of reactive oxygen species and mitochondrial DNA (mtDNA) [15]. These molecules act as danger signals, triggering pathological processes in the surrounding environment [16]. Mitochondrial dysfunction has been implicated in the pathogenesis of alcoholic fatty liver disease (ALFLD), metabolic dysfunction-associated steatotic liver disease (MASLD) and related inflammation [17, 18].

Recent studies highlight a sophisticated mitochondrial quality control system involving mitochondria-derived vesicles (MDVs) [19]. Under stress conditions, damaged mitochondria generate MDVs through mtDNA-membrane fusion events. These vesicles shuttle selected mitochondrial cargo to target organelles and neighboring cells. To maintain intracellular homeostasis, mitochondria utilize a quality control system. MDVs containing damaged mitochondrial components are transported to lysosomes for degradation, a process reliant on the Parkinson's disease-related protein, Parkin [20]. Alternatively, with the assistance of the Snx9 protein, MDVs are directed to the cell membrane, where they are secreted as exosome vehicles (EVs) after membrane fusion, facilitating intercellular communication and potentially contributing to antigen presentation [21].

In macrophage-driven inflammatory responses, the cyclic GMP-AMP synthase (cGAS)-stimulator of interferon genes (STING) axis has emerged as a critical sensor of hepatocyte-derived mtDNA. Upon activation, cGAS dimerizes and synthesizes the dinucleotide second messenger 2′,3′-cyclic GMP-AMP (cGAMP), which binds with high affinity to the stimulator of interferon genes (STING) in the endoplasmic reticulum. This interaction drives inflammatory responses [22]. The cGAS-STING signaling pathway has been implicated in various chronic diseases, mediating aberrant signaling that promotes disease progression [23]. However, mechanistic insights into how mtDNA released from stressed hepatocytes engages macrophage cGAS-STING signaling, and its potential regulatory effects on MDBs pathogenesis, represent significant gaps in current understanding.

In this study, single-nucleus RNA sequencing (snRNA-seq) analysis revealed significant activation of the TGF-β/TGF-βR ligand-receptor pair in our dataset. We further investigated the role of JNK pathway activation in driving MDBs formation and inducing an inflammatory

environment through mitochondrial damage and subsequent mtDNA release to macrophages. Mechanistically, JNK pathway inhibition was found to suppress MDBs formation by downregulating c-JUN transcription and mitigate inflammation by reducing mitochondrial damage. Analysis of clinical metabolic associated fatty liver disease (MAFLD) datasets corroborated the activation of the TGF-β/JNK axis in chronic liver disorders. Our findings provide novel insights into the pathogenesis of MDBs, highlighting the TGF-β/JNK signaling axis as a potential therapeutic target for chronic liver diseases.

Materials and methods

Ethics statement and clinical specimen acquisition

Formalin-fixed paraffin-embedded (FFPE) liver biopsies from patients with HCC (n = 10) were obtained from the archives of Qingyuan Affiliated Hospital of Guangzhou Medical University, following Institutional Review Board approval (IRB-2022–094). Cases with significant MDBs (n = 3) were selected and evaluated by experienced pathologists (Table S1). The study adhered to the principles of the Declaration of Helsinki, with data analyzed anonymously. All procedures involving human sample collection were approved and registered at Medicalresearch.org.cn by the tissue bank of the Qingyuan Affiliated Hospital of Guangzhou Medical University (ChiCTR2400084248). Informed consent was obtained from all participants.

Animal experiments

Male mice of the C3H background were purchased from Beijing Vital River Laboratory Animal Technology and housed in specific-pathogen-free (SPF) conditions at Guangzhou Medical University. The mice were maintained at 20–26 °C and 40–70% humidity under a 12-h light/dark cycle with free access to food and water. Experimental protocols were approved by the Animal Care Committee of Guangzhou Medical University (GY2022144).

Control mice (n = 3) were fed a standard diet, while the MDB-induction model was generated by feeding mice a diet supplemented with 0.1% 3,5-diethoxycarbonyl-1,4-dihydrocollidine (DDC, Sigma-Aldrich, 137,030-25G) for 10 weeks (n = 3). After 10 weeks, a withdrawal period of one month was applied (n = 3), during which MDBs largely disappeared. Mice were then re-fed DDC for 6–10 days to reinduce MDBs formation, as described previously [24].

Single-nucleus RNA-sequencing (snRNA-seq)

Nuclei isolation and snRNA-seq were performed using the 10 ×Genomics® protocol, with data analysis conducted by Genedenovo Biotechnology Co., Ltd (Guangzhou, China). Quality control and clustering analysis were performed using the Seurat R package. Ligand-receptor interactions between cell types were analyzed using *CellphoneDB*. Gene Set Variation Analysis (GSVA) was utilized for pathway enrichment analysis, comparing active cellular pathways between DDC-treated and control groups.

Identification of differentially expressed genes (DEGs)

Differentially expressed genes (DEGs) between NAFLD patients and healthy controls were identified using the *limma* package. DEGs were selected based on a p-value < 0.05 and a fold change (FC) > 1 in absolute value.

Weighted gene co-expression network analysis (WGCNA)

Microarray datasets for MASLD were obtained from the NCBI Gene Expression Omnibus (GEO) database (http://www.ncbi.nih.gov/geo/), with GSE260666 selected for analysis. Using the WGCNA package, an optimal soft threshold power (β) was determined, and co-expression modules were identified via the one-step network construction method. The module with the highest expression was subjected to GO enrichment analysis, and its genes were cross-referenced with previously identified DEGs to identify hub genes.

Generation of UbD KO mice and treatment

UbD knockout ($UbD^{-/-}$) C3H mice were generated using CRISPR/Cas9 technology as previously described [25]. $UbD^{-/-}$ and wild-type (WT) mice were fed a 0.1% DDC-supplemented diet for 8 weeks. Liver tissues and blood samples were collected from each group (n = 3) for further analysis. Animal experiments were approved by the Institutional Animal Care and Use Committee of Guangzhou Medical University (GY2022-101).

Hematoxylin and Eosin (H&E) staining

Liver sections were deparaffinized using TO, rehydrated through graded alcohols, and stained in hematoxylin solution for 3 min. After washing with 0.1% Tween-20 in PBS for 5 min, the sections were stained in eosin solution for 2 min to visualize the cytoplasm. Following a 5-min rinse in tap water, the sections were dehydrated, and mounting medium was applied for coverslip placement. Images were captured using the PRECICE 500 slide scanner system (UNIC) and processed with *iViewer* software (UNIC).

Immunohistochemical assay

Liver sections were deparaffinized using TO and rehydrated with graded alcohols. Antigen retrieval was performed via microwave heating in citrate antigen retrieval solution (Beyotime, P0081). Sections were fixed in 4%

paraformaldehyde for 15 min and blocked with 5% BSA for 1 h at room temperature (RT). Mouse anti-F4/80 antibody (Bioss, bsm-34028 M) was applied overnight at 4 °C. After washing, sections were incubated with HRP-conjugated secondary antibodies for 1 h at RT, and signals were detected using a DAB kit (ZSGB-Bio, ZLI-9018). Counterstaining with hematoxylin was performed before image capture using the PRECICE 500 slide scanner (UNIC) and analysis with iViewer software (UNIC).

Serum biochemistry assay

Serum samples from mice in each group were analyzed. Aspartate transaminase (AST) and alanine aminotransferase (ALT) levels were measured using standard procedures at Wuhan Servicebio Biotechnology Co., Ltd (China).

RNA extraction and quantitative PCR (qPCR)

Total RNA was extracted from tissues or cells using the Cell/Tissue Total RNA Kit (Yeason, 19221ES50) and reverse-transcribed into cDNA using 5× HiScript III qRT SuperMix (Vazyme, R323-01). Quantitative PCR was performed using TB Green® Premix Ex Taq™ II (TaKaRa, RR820 A) with primers listed in Table S2.

Immunofluorescence (IF)

Paraffin-embedded liver sections were dewaxed, subjected to antigen retrieval, and blocked with 5% BSA for 1 h at RT. Autofluorescence was quenched using a tissue autofluorescence quencher (Servicebio, G1221), followed by washing with 0.1% Tween-20 in PBS three times (3 min each). Sections were incubated overnight at 4 °C with primary antibodies: rabbit anti-F4/80 (Bioss, bsm-34028 M), rabbit anti-cGAS (Proteintech, 29,958–1-AP), rabbit anti-STING (Proteintech, 19,851–1-AP), and mouse anti-DNA (Progen, 61,014). After washing, sections were incubated for 1 h with Alexa Fluor™-conjugated secondary antibodies (Invitrogen): Goat anti-Rabbit IgG Alexa Fluor™ 488 (A11008), Goat anti-Mouse IgG Alexa Fluor™ 488 (A11001), Goat anti-Rabbit IgG Alexa Fluor™ 555 (A21428), and Goat anti-Mouse IgG Alexa Fluor™ 555 (A21422). Sections were stained with DAPI (Beyotime, C1002) for 5 min, washed with 0.1% Tween-20 in PBS, and mounted with Antifade Mounting Medium (Beyotime, P0128M). Images were captured using a ZEISS LSM880 laser confocal microscope and processed with ZEN software (ZEISS).

Transmission electron microscopical analysis

Liver tissues from control and experimental groups were cut into 1–3 mm sections and fixed with 2.5% glutaraldehyde (pH 7.4) for 2 h. After washing three times with 0.1 M phosphate buffer (pH 7.2), tissues were fixed with 1% osmium tetroxide at 4 °C for 2 h. Sections were dehydrated with graded alcohols and embedded in Epon-Araldite resin (Ted Pella Inc). Ultrathin sections were prepared using a Leica EM UC7 Ultramicrotome and counterstained with 3% uranyl acetate and 2.7% lead citrate. Sections were examined using a JEM1400 transmission electron microscope (JEOL, JEM1400).

Induction of MDBs in vitro

Hepa1-6 cells were co-stimulated with 40 ng/ml TNF-α (PeproTech, 315-01 A) and 400 ng/ml IFN-γ (Novoprotein, C746) for 10 days, with medium replacement every three days, as previously described [26]. On day 10, cells were harvested for subsequent experiments. To simulate in vivo TGF-β release, TGF-β (5 ng/ml, Novoprotein, C3036) was added for 12, 24, or 48 h. For treatments involving JNK-IN-8 (MCE, HY-13319), cells were pretreated with JNK-IN-8 for 90 min before co-stimulation with TGF-β for 24 h. Control groups included a blank group treated with DMSO and an untreated control group. After culture, cells were quantified, and target protein expression levels were analyzed using Western blot or immunofluorescence (IF).

Western blot analysis

Proteins were extracted from frozen liver tissues or cell samples using RIPA lysis buffer (Beyotime, P0013B) supplemented with a protease inhibitor cocktail (Apexbio, K1007) and a phosphatase inhibitor cocktail (Apexbio, K1015). Lysates were mixed with 5× SDS loading buffer, denatured at 100 °C for 10 min, separated on SDS-PAGE (10% or 12% polyacrylamide gels), and transferred to PVDF membranes (Millipore, ISEQ00010). Membranes were incubated with primary antibodies against proteins, including anti-c-JUN (Proteintech, 24,909–1-AP), anti-JNK (CST, 9252 T), anti-Phospho-SAPK/JNK (Thr183/Tyr185, CST, 4668 T), anti-TOM20 (Proteintech, 11,802–1-AP), anti-BAX (Proteintech, 50,599–2-Ig), anti-BAK (Proteintech, 29,552–1-AP), anti-cGAS (Proteintech, 29,958–1-AP), anti-STING (Proteintech, 19,851–1-AP), anti-K8 (Proteintech, 17,514–1-AP), anti-p62 (Proteintech, 66,184–1-Ig), and anti-GAPDH mouse mAb (Proteintech, 60,004–1-Ig). HRP-conjugated secondary antibodies were used for detection, and signals were visualized using chemiluminescence imaging systems Pxi9 (Sysgene) or Amersham Imager 680 (GE). Image analysis was performed using ImageJ software.

Enzyme-linked immunosorbent assay (ELISA)

Levels of cytokines and chemokines (TGF-β and IL-6) were measured using ELISA kits according to the manufacturer's protocols (Thermo Fisher Scientific).

Data were analyzed using GraphPad Prism version 9.0 (GraphPad Software, California, USA).

Dual luciferase reporter assay

Potential c-JUN binding sites on the UbD promoter were identified using the transcription factor database Jaspar (https://jaspar.elixir.no). UbD promoter fragments (Full, Mut1, Mut2, and Mut3) were cloned into the pGL3-basic vector, and the c-JUN coding sequence was inserted into the pcDNA3.4 vector (Igebio, China). HEK-293 T cells were seeded in 24-well plates at a density of 1.0×10^5 cells/well and co-transfected with firefly luciferase plasmids (h-UbD Full, Mut1, Mut2, Mut3, or pGL3-Basic as a negative control), the c-JUN expression vector (h-c-JUN or pcDNA3.4), and the pRL-TK Renilla luciferase vector (internal control). When cells reached 60–70% confluence, luciferase activity was measured 48 h post-transfection using the Dual-Luciferase Reporter Assay Kit (Promega, E1910). Luminescence signals were detected with a multifunctional microplate reader (Varioskan Flash, Thermo, USA). Experiments were repeated three times. The sequences of the UbD and c-JUN plasmids are provided in Table S3.

Flow cytometry

Livers were collected from mice post-euthanasia and minced using surgical scissors. The tissue fragments were incubated in 5–10 ml of DMEM containing 200 U/ml collagenase IV (Gibco, 17,104,019) at 37 °C on a thermostatic shaker (New Brunswick Scientific, EXCELLA E24R) at 200 rpm for 1 h. The resulting cell suspension was filtered through a 100 μm sieve, and the filtrate was collected in a 50 ml centrifuge tube. PBS was added to reach 50 ml, and the suspension was centrifuged at 500 ×*g* for 3 min. The cell pellet was resuspended in red blood cell lysis buffer (BioLegend, 420,301) and incubated for 5–10 min at room temperature. Lysis was terminated by adding three times the volume of PBS, followed by centrifugation at 500 ×*g* for 3 min. The resulting cell pellet was resuspended in FACS buffer (PBS with 2% FBS).

Cells were activated with 500 ng/ml LPS (Absin, abs4701484) overnight, and brefeldin A (BD Pharmingen, 555,029) was added for the final 5 h before intracellular staining. Fixed cells were incubated with antibodies against CD45 (BD Pharmingen, 561,037), CD11b (BD Pharmingen, 570,293), F4/80 (BioLegend, 123,107), IL-6 (BioLegend, 504,503), and TGF-β (BD Pharmingen, 565,638). After staining, cells were resuspended in 200–400 μl FACS buffer and analyzed using flow cytometry (BD FACS Verse).

Isolation of primary KCs

The liver cell suspension was centrifuged at 500 ×*g* for 3 min, and the supernatant was discarded. The cell pellet was resuspended in 20 ml DMEM medium and centrifuged at 500 ×*g* for 3 min, repeated twice. Next, the pellet was resuspended in 20 ml DMEM medium and centrifuged at 50 ×*g* for 3 min. The supernatant was collected in a fresh 50 ml tube, and this step was repeated three times to obtain approximately 50 ml of supernatant. The combined supernatant was centrifuged at 500 ×*g* for 3 min, and the supernatant was discarded. The cell pellet was washed with PBS, centrifuged at 500 ×*g* for 3 min (repeated twice), resuspended in DMEM containing 10% FBS, and plated in six-well plates. After 2 h, the medium was replaced, wells were washed with PBS, and fresh medium was added.

Tissue mitochondrial isolation

Fresh liver tissues were homogenized and processed using the Tissue Mitochondrial Isolation Kit (Beyotime, C3606). The homogenate was centrifuged at 800 ×*g* for 5 min, and the supernatant was transferred to a new 1.5 ml microcentrifuge tube. This was followed by centrifugation at 8000 ×*g* for 10 min to isolate the mitochondrial pellet.

(See figure on next page.)

Fig. 1 MDBs formation is accompanied with TGF-β release during chronic liver injury. **A** MDBs formation mouse model was induced by 0.1% DDC (n = 3). Modeled Mice were sacrificed at 10-, 14-, and 15-week intervals for liver sampling. Then the mice livers in each treatment group were prepared into single cell suspensions for snRNA sequencing analysis. **B** Representative morphologies of livers are shown. **C** Liver weights of indicated mice were quantified and normalized to body weight. All data were representative of at least three-independent experiments. **D**, **E** Biochemical assay of serum ALT and AST. Data are presented as mean ± SD; Statistical significance was assessed by Student's t test. **F**, **G** Histopathological assessment by H&E and Oil Red O staining. MDBs was counted in multiple fields of view in HE-stained sections, as indicated by yellow arrows. Meanwhile, 6 randomly selected visual field MDBs were counted and statistically analyzed. Bar = 100 μm. **H** Transmission electron microscopy of MDB ultrastructure. bar: 2 μm. **I** Cell to cell crosstalk analysis of Control and DDC-Fed group, depicting interactions among 9 hepatic cell subtypes. **J** SnRNA-seq analysis of ligand-receptor pair dynamics in control and DDC-Fed group. **K** The secretion of TGF-β of macrophages in DDC-induced MDBs mouse livers was assayed by flow cytometry. **L** Serum TGF-β levels measured by ELISA. **M** The mRNAs of TGF-β, TGF-βR1 and TGF-βR2 in MDBs mouse livers were determined by qPCR analysis (n = 3)

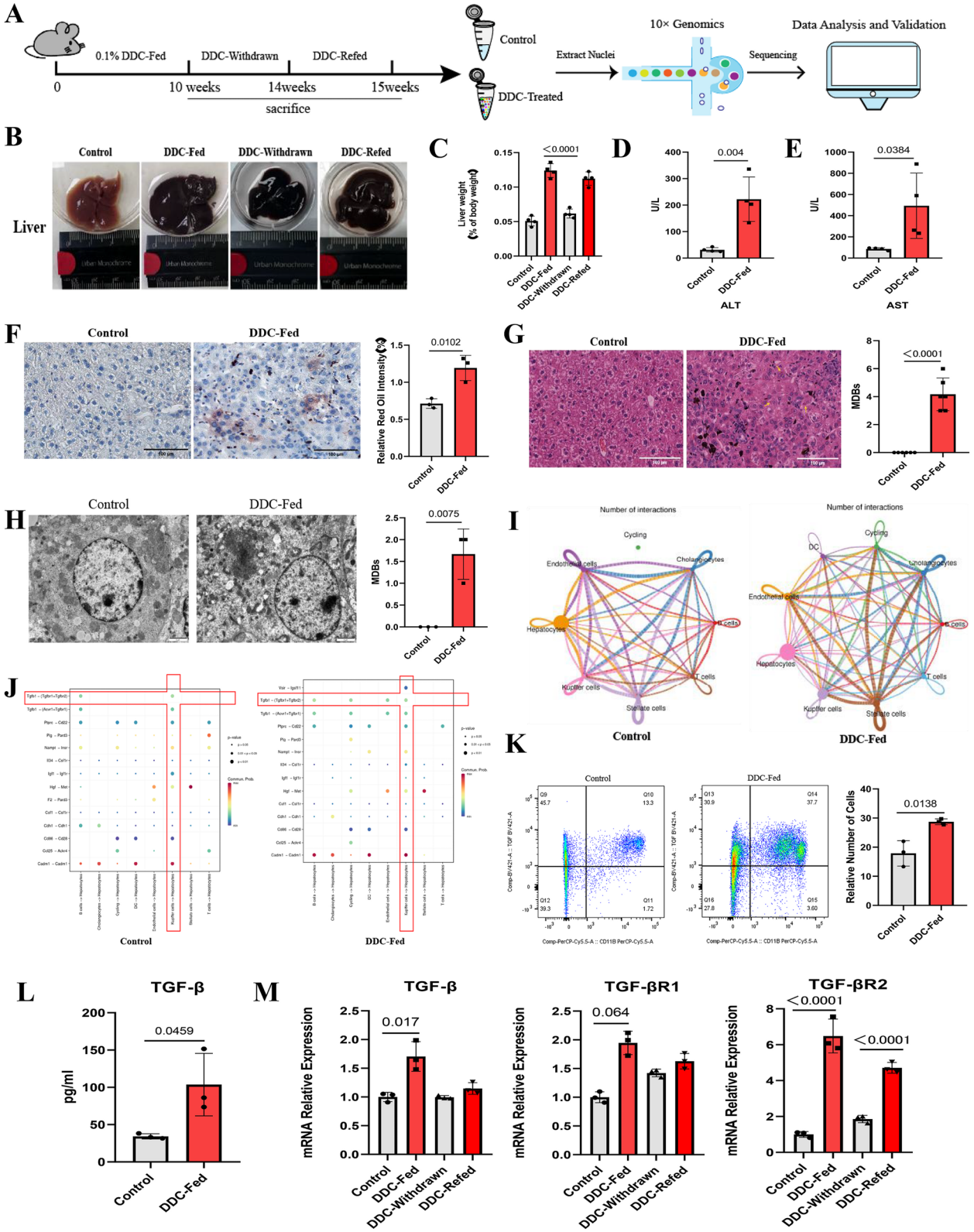

Fig. 1 (See legend on previous page.)

Quantification of inflammatory responses

To evaluate the proinflammatory effects of extracellular mitochondrial components, isolated mitochondria (120 μg) were added to 1×10^6 RAW264.7 cells for 16 h, as described by Todkar et al. [20]. After incubation, cells were collected, and total RNA was extracted for reverse transcription into cDNA. Quantitative PCR (qPCR) was performed to measure the mRNA levels of IL-6.

Co-culture of Hepa1-6 and RAW264.7 cells

RAW264.7 cells were seeded at a density of 8×10^6 cells per well in 24-well plates and incubated overnight. Hepa1-6 cells pretreated under different conditions were seeded into Transwell inserts (LABSELECT, 14,322) at a density of 8×10^6 cells. The inserts were placed into wells containing RAW264.7 cells for co-culture for 24 h (three replicates per group). After co-culture, RAW264.7 cells were collected from the lower chamber for further analysis.

Statistical analysis

All data in this study are presented as mean ± SEM or SD from three independent experiments. A P-value of <0.05 was considered statistically significant. Statistical analyses were performed using GraphPad Prism version 9.0 (GraphPad Software, California, USA).

Data availability

The single-nucleus RNA sequencing (snRNA-seq) data generated in this study have been deposited in the GEO database under accession number GSE201569. For details on GEO data linking and citation, please refer to: https://www.ncbi.nlm.nih.gov/geo/info/linking.html. The data are also available from the corresponding author upon reasonable request.

Results

MDBs formation is accompanied by the release of TGF-β

As detailed in the "Materials and methods" section, we established an animal model for stable MDBs formation by DDC feeding, following our previous methods [24]. Using single-nucleus RNA sequencing (snRNA-seq), we performed an in-depth analysis of the complex mechanisms underlying MDBs formation in normal and drug-fed mice (Fig. 1A). DDC-fed mice exhibited weight loss, liver enlargement, darkened liver coloration, and hardened texture (Fig. 1B, C). Elevated serum levels of alanine aminotransferase (ALT) and aspartate aminotransferase (AST) confirmed liver injury induced by DDC (Fig. 1D, E). Additionally, Oil Red O staining revealed increased liver necrosis in DDC-fed mice (Fig. 1F).

Multimodal histopathological evaluation combining HE staining and electron microscopy revealed pronounced MDBs deposition within hepatocytes of DDC-induced murine models. (Fig. 1G, H). Strikingly, snRNA-seq data revealed substantial variability among hepatocyte and macrophage subpopulations after DDC feeding, along with enhanced intercellular communication between these cells (Fig. 1I, Figs. S1 and S2). Analysis of ligand-receptor interactions identified the TGF-β/TGF-βR axis as significantly enriched in hepatocyte-macrophage communication in DDC-treated mice (Fig. 1J, Fig. S3), implicating this pathway in MDBs formation.

Flow cytometry analysis showed a twofold increase in TGF-β release by macrophages in MDB-affected livers compared to controls, confirming macrophages as the primary source of TGF-β during this process (Fig. 1K). ELISA further confirmed elevated serum TGF-β levels in DDC-fed mice (Fig. 1L), and mRNA expression of TGF-β receptors (TGF-βR1 and TGF-βR2) was significantly upregulated during MDBs pathogenesis (Fig. 1M). These findings indicate that MDBs formation is accompanied by TGF-β release, highlighting the critical role of the TGF-β/TGF-βR axis in chronic liver injury.

WGCNA analysis of TGF-β/JNK axis activation in clinical MASLD (NAFLD) patients

To investigate the activation of the TGF-β/JNK axis in clinical liver disorders, we analyzed microarray data (GSE260666) from the GEO database. Weighted Gene Co-expression Network Analysis (WGCNA) was performed on six healthy controls and ten MASLD patients (Fig. 2A) following established methods [27].

Transcriptional profiles from MASLD patients displayed distinct characteristics compared to healthy

(See figure on next page.)

Fig. 2 WGCNA uncovers the activation of the TGF-β/JNK axis in MASLD (NAFLD) patients. **A** Computational workflow for WGCNA implementation on transcriptomic data from 10 clinically confirmed MASLD patients and 6 age-matched controls. **B** The heatmap illustrating the genes with the highest standard deviation changes among individuals diagnosed with MASLD and normal controls. **C** The soft threshold power and mean connectivity of WGCNA network. **D** The cluster dendrogram of WGCNA network. **E** The heatmap depicting the relationship between the modules and clinical traits. **F** The dot plot showing the top 20 enriched reactome pathways of the "turquoise" module. **G** The venn diagram of the intersection of DEGs, "turquoise" module genes. **H** Percentage sharing of these 7 hub genes in each cell subpopulation after DDC feeding. **I** mRNAs analysis of SOD2, YARS, MARS and FNDC4 in DDC-treated and control group

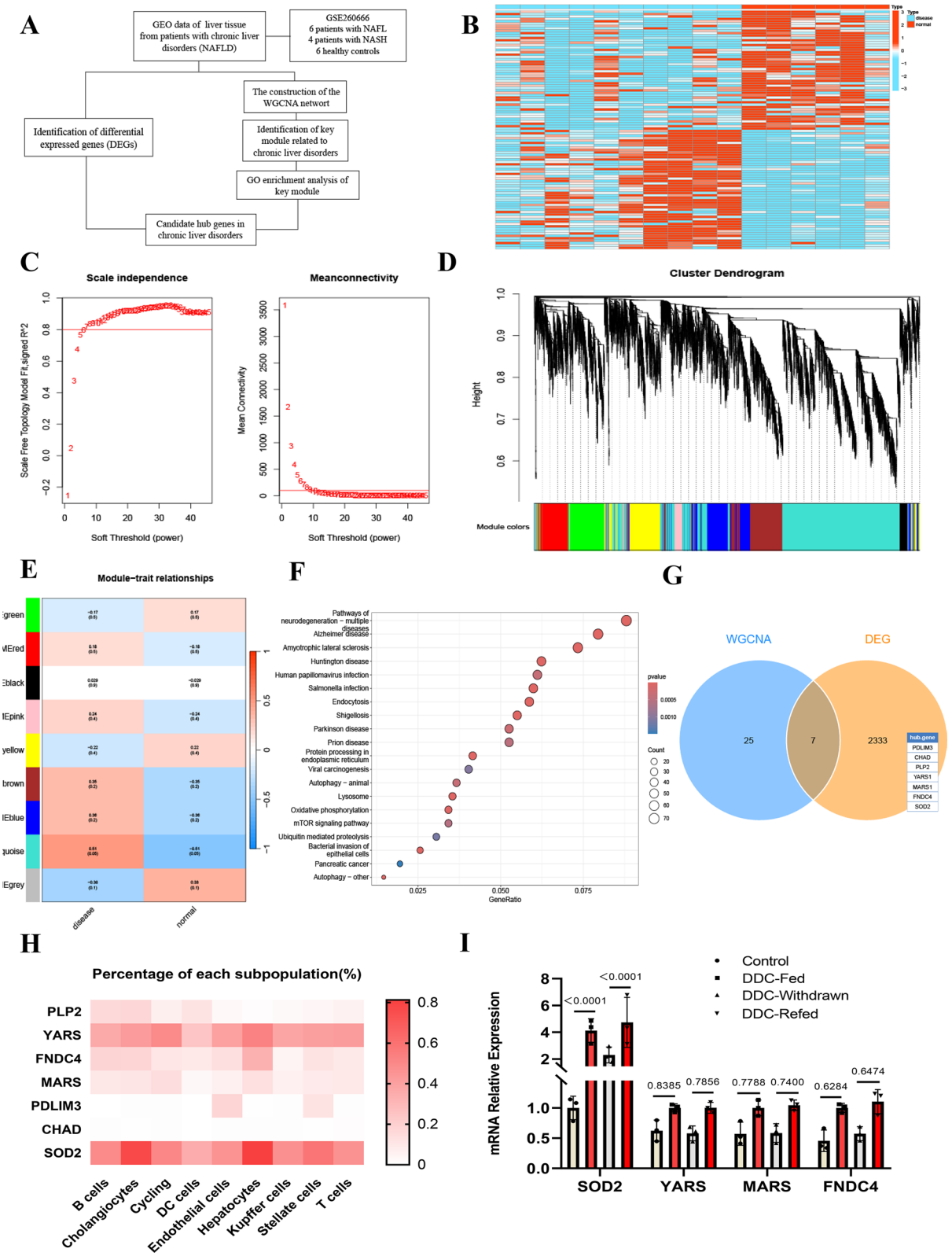

Fig. 2 (See legend on previous page.)

controls, indicating unique molecular features of MASLD (Fig. 2B). A soft threshold of 6 was selected to ensure scale-free network topology, as confirmed by model fit and connectivity analysis (Fig. 2C). We identified nine gene modules with distinct co-expression patterns (Fig. 2D). The "turquoise" module exhibited the highest correlation with MASLD (correlation coefficient: 0.51, p-value < 0.05) (Fig. 2E).

WGCNA analysis identified significant enrichment of neurodegenerative-associated pathways—particularly Alzheimer's disease—in the turquoise module through Gene Ontology (GO) profiling, revealing conserved pathomechanistic features between MDBs pathogenesis and neurodegenerative proteinopathies (Fig. 2F). Additionally, the enrichment of the ubiquitin–proteasome pathway suggested a role for protein misfolding in MASLD-related MDBs formation. Autophagy, oxidative phosphorylation, and lysosomal pathways were also enriched, indicating shared mechanisms between clinical MASLD and animal models of MDBs formation (Fig. 2F, Fig. S4).

Genes identified as differentially expressed (DEGs) and present in the turquoise module were considered hub candidates for MASLD (Fig. 2G). Among these, SOD2, YARS, MARS, and FNDC4 were upregulated in both animal model and clinical datasets (Fig. 2H). Their mRNA upregulation was further validated experimentally (Fig. 2I). Notably, SOD2 has been shown to mediate liver disorders via the TGF-β/JNK axis [9, 15, 28].

Through integrative analysis of clinical MASLD data, we provide clinical validation for the pathological activation of the TGF-β/JNK signaling cascade, establishing its mechanistic rationale as a novel therapeutic target for mitigating MDBs formation and arresting disease progression in chronic liver disorders.

TGF-β activates the JNK signaling pathway and its cascade response

Gene Set Variation Analysis (GSVA) enables systematic investigation of disease progression mechanisms through pathway-level genomic signature quantification. Analysis of GSVA results revealed significant upregulation of the TGF-β signaling pathway in DDC-fed and refed groups (Fig. 3A). TGF-β signal transduction stimulates diverse cellular responses and plays a critical role in numerous pathophysiological processes [29]. Mechanistically, TGF-β signaling activates the downstream MAPK pathway in processes such as epithelial-mesenchymal transition (EMT) and autophagy [8, 30].

Western blot analysis showed significant activation of the JNK pathway in DDC-treated groups (Fig. 3B). Single-cell regulatory network inference and clustering (SCENIC) analysis further revealed high expression of the transcription factor c-JUN in experimental groups (Fig. 3C), particularly within the hepatocyte subpopulation (Fig. 3D). Elevated c-JUN expression was confirmed at both mRNA and protein levels in MDBs mouse livers and MDB-associated HCC tissues (Fig. 3E–G).

Employing a TNF-α and IFN-γ-primed Hepa1-6 MDBs formation model (Fig. S5), we observed that c-JUN and phosphorylated JNK (p-JNK) were activated 24 h after TGF-β addition, indicating that TGF-β triggers JNK pathway activation (Fig. 3H). These phosphorylation patterns demonstrate TGF-β's capacity to initiate JNK pathway signaling preceding MDBs pathogenesis.

c-JUN promotes MDBs formation via UbD upregulation, which was repressed in UbD$^{-/-}$ mice

Ubiquitin D (UbD) is highly expressed in hepatocellular carcinoma and has been proposed as a potential marker for MDBs [26]. Similarly, K8 and p62 proteins are significantly upregulated in MDB-forming livers [31]. Our results showed simultaneous expression of UbD, K8, and p62 in hepatocyte subpopulations of MDB-forming livers (Fig. 4A and Fig. S6, 7), with qPCR confirming significant upregulation of UbD mRNA in DDC-treated groups (Fig. 4B). Enhanced co-localization of K8 and p62 was observed in DDC-fed groups (Fig. 4C).

To explore the regulation of UbD by c-JUN, promoter analysis using JASPAR software predicted multiple c-JUN binding sites within the UbD promoter (Fig. 4D). Subsequent functional validation through dual-luciferase reporter systems validated a induction of transcriptional activation following c-JUN overexpression compared

(See figure on next page.)

Fig. 3 Significant activation of the JNK pathway and transcriptional initiation of c-JUN. **A** GSVA analysis of upregulated pathways in DDC-treated and Control group. **B** Liver lysates of DDC-treated and Control group were analyzed by Western blot. All data are representative of three independent experiments. Bands were analyzed for grayscale values by ImageJ and quantified by using Prism software. **C** Heatmap visualization of differentially expressed transcription factors in DDC-treated and Control group. **D** Percentage ratio changes of c-JUN in each cell subpopulation after DDC feeding. **E** RT-qPCR analysis of c-JUN mRNA levels normalized to GAPDH. **F**, **G** Liver lysates of DDC-treated and Control group and clinical MDB-formed HCC samples (n = 3) were analyzed by Western blot. **H** Cells was stimulated for 12, 24 and 48 h after TGF-β addition in vitro MDBs cell model. Then cellular proteins were collected and cell lysates were analyzed by Western blot using the antibodies against p-JNK、total JNK and c-JUN. α-tubulin served as a loading control. All data were representative of at least three-independent experiments. Bands were analyzed for densitometry quantification

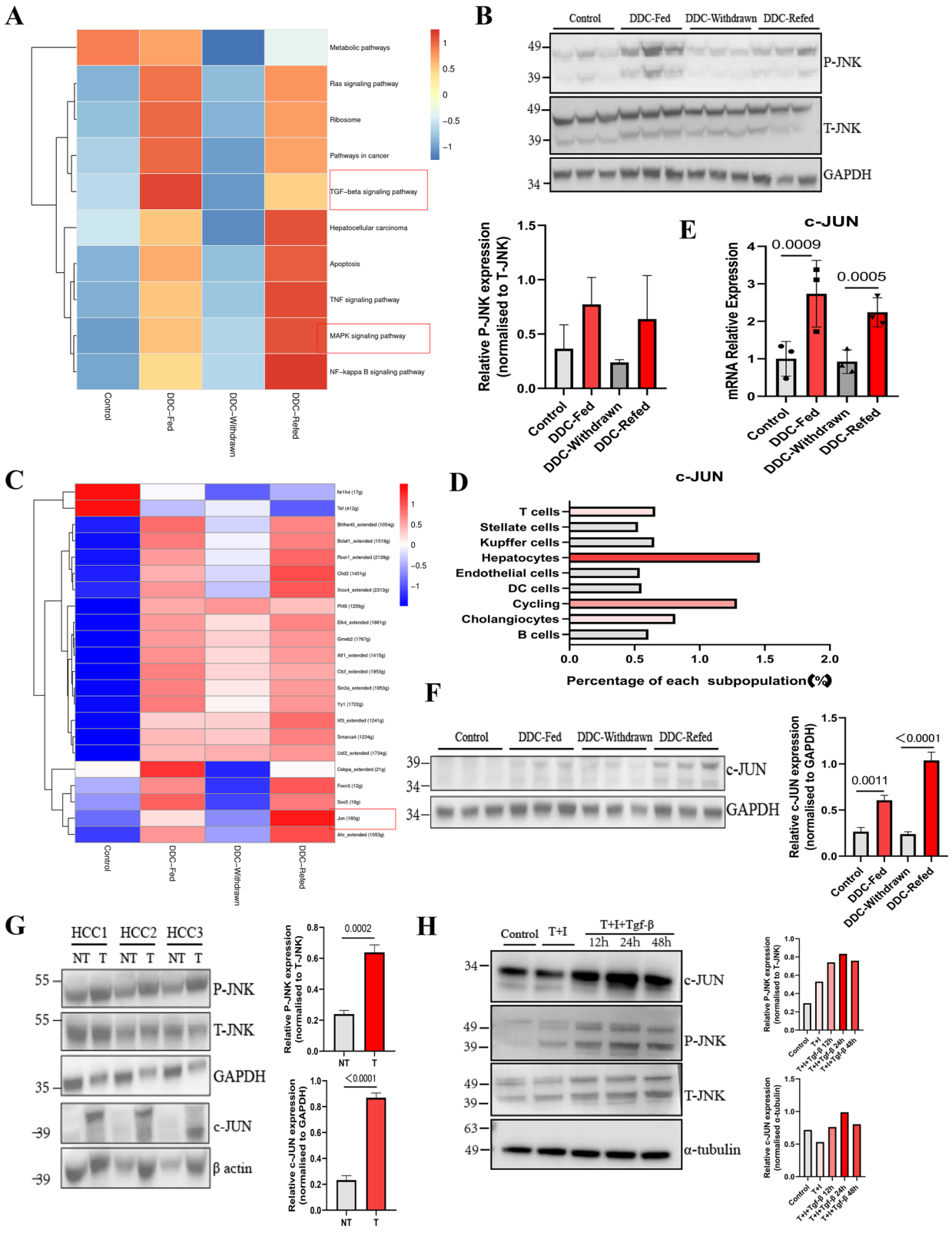

Fig. 3 (See legend on previous page.)

to pcDNA3.4-pGL3-UbD group (Fig. 4E). Mutations in c-JUN binding sites (pGL3-mut1/mut2/mut3) led to reduced fluorescence activity, which was restored by c-JUN overexpression (Fig. 4E).

To further validate the role of UbD, we generated UbD-knockout (UbD-/-) mice. Knockout of UbD resulted in significantly decreased mRNA levels of K8, p62, and c-JUN (Fig. 4G), along with reduced co-localization of K8 and p62, as shown by immunofluorescence (Fig. 4H). Western blot analysis confirmed decreased c-JUN protein levels in DDC-induced $UbD^{-/-}$ mice (Fig. 4I).

Collectively, these findings establish a strong association between c-JUN and UbD, demonstrating that c-JUN promotes MDBs formation by directly regulating UbD expression.

Chronic liver injury was associated with mitochondrial damage and the formation of MDVs

Mitochondria are critical organelles for maintaining cellular homeostasis and have garnered increasing attention due to functional changes observed in various pathological conditions [32]. Ultrastructural analysis by transmission electron microscopy revealed distinct mitochondrial signatures in our MDB-forming model [33] (Fig. 5A). In the control group, the mitochondrial bilayer membrane remained structurally intact, and mitochondrial cristae were organized in homogeneous rows, with an arrow indicating a normal lysosome. In contrast, the experimental group showed mitochondrial membrane rupture, vacuolar degeneration, and disorganized cristae, accompanied by the initiation of autophagic lysosomes (Fig. 5A).

Ultrastructural profiling revealed the membranous structures, known as MDVs, harboring selectively packaged mitochondrial membrane constituents. Intriguingly, a significant number of these MDVs evaded lysosomal degradation. Subsequently, TEM captured their dynamic docking at plasma membrane microdomains, primed for extracellular release as bioactive EVs capable of executing intercellular mitochondrial signaling (Fig. 5B). Two main processing pathways for the release of damaged mitochondrial products during MDBs formation are illustrated (Fig. 5C). These results suggest that systematic control of mitochondrial homeostasis is initiated during MDBs pathogenesis, similar to other injury conditions [34].

The TOM20 protein, a mitochondrial outer membrane protein, was upregulated upon DDC treatment (Fig. 5D), a finding that was also verified in the MDB-forming Hepa1-6 cell model (Fig. 5E). Furthermore, we confirmed that TOM20 and mtDNA breakage co-localized in MDBs liver tissues (Fig. 5F and Fig. 5H) and MDB-forming Hepa1-6 cells (Fig. 5G, H). In the negative control group, TOM20 was tightly arranged, and mtDNA expression was weak. In contrast, in MDBs pathogenesis, the TOM20-labeled outer membrane structure was fractured, and mtDNA was released (Fig. 5F, H). Taken together, these findings indicate that chronic liver injury is typically accompanied by mitochondrial membrane rupture, with mtDNA and the ruptured outer membrane protein TOM20 secreted as mitochondrial inclusions during MDBs formation.

MDBs pathogenesis was accompanied by MDVs release through BAX/BAK pore formation

GSVA analysis indicated that the process of MDBs formation was associated with the activation of the apoptosis pathway (Fig. 6A). BAX and BAK, classical pro-apoptotic molecules in the apoptotic pathway, are frequently regulated by the JNK signaling pathway [35, 36]. Mitochondrial outer membrane permeabilization (MOMP) has been shown to have various pro-inflammatory functions [37]. While MOMP is typically induced in the context of apoptosis, we hypothesized that under stress conditions, cytosolic BAX would migrate to the mitochondrial membrane, where it would form a BAX/BAK pore with upregulated BAK to facilitate the release of MDVs carrying mtDNA. This process would be accompanied by MOMP in the livers of MDB-injured mice (Fig. S8).

We firstly validated that both BAX and BAK were upregulated at the mRNA and protein levels in MDBs livers and MDB-forming liver cells (Fig. 6B–D). Then, we isolated mitochondrial and cytosolic proteins from the livers of normal and DDC-fed mice. As expected, BAX protein levels were elevated in both the cytosol and mitochondria under DDC injury, and the amount of BAK

(See figure on next page.)

Fig. 4 c-JUN is directly involved in regulating UbD expression while was repressed in DDC-induced $UbD^{-/-}$ mice. **A** Percentage sharing of UbD、K8 and p62 in each cell subpopulation after DDC feeding. **B** RT-qPCR analysis of UbD, K8, and p62 mRNA levels normalized to GAPDH. **C** Immunofluorescence co-localization analysis of K8 and p62 in liver sections. Nuclei counterstained with DAPI (n = 3). Bar = 100 μm. **D** Jaspar software predicts that UbD promoter contains multiple binding sites of c-JUN. **E** Dual-luciferase reporter assay demonstrating c-JUN-mediated UbD transcriptional activation. **F** Schematic diagram of UbD knockout mice construction. **G** Validation of UbD、K8、p62 and c-JUN in mRNA level changes in WT/$UbD^{-/-}$ mice by qPCR analysis. **H** IF confirms the effect of K8 and p62 expression levels and degree of co-localization in WT/$UbD^{-/-}$ mice. Three fields of view were randomly selected and analyzed for fluorescence intensity quantification. Bar = 100 μm. **I** Liver lysates of $UbD^{-/-}$ mice samples (n = 3) were analyzed by Western blot using antibodies against c-JUN. α-tubulin served as a loading control

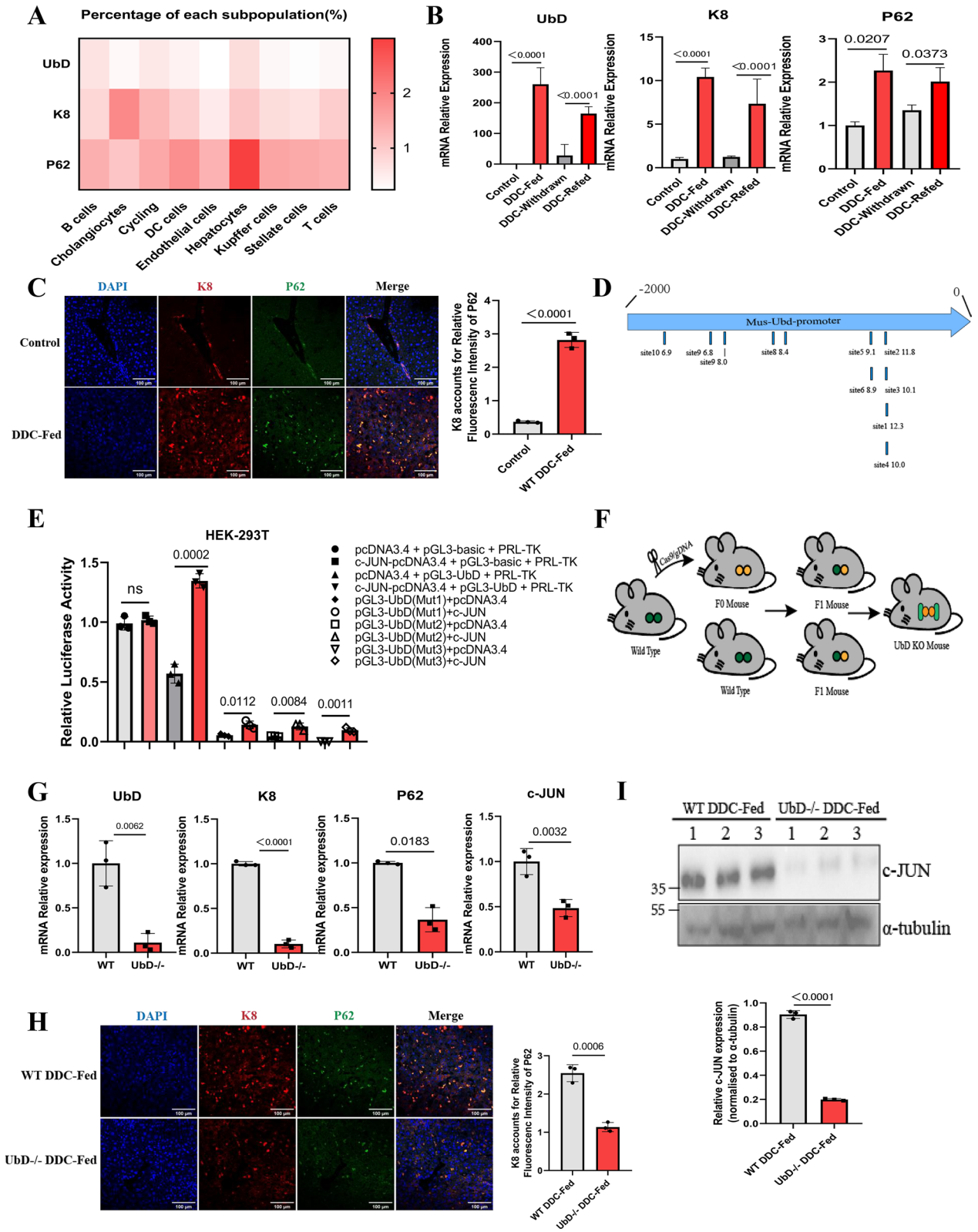

Fig. 4 (See legend on previous page.)

expressed in mitochondria also increased. Similarly, the expression of BAX and BAK in withdrawn/refed groups mirrored the trend observed in control and DDC-fed groups (Fig. 6E).

We further performed immunofluorescence (IF) analysis on mouse liver tissue, which revealed increased orientation of BAK toward the mitochondrial membrane following DDC feeding. This was accompanied by ruptured mtDNA structures that fused with BAK (Fig. 6F). These results demonstrate that JNK activation during MDBs formation induces BAX/BAK oligomerization, generating mitochondrial pores that mediate MDVs extrusion containing mtDNA. And this process coincides with MOMP.

mtDNA accumulation activates cGAS-STING inflammatory response during MDBs formation

As established, non-degraded MDVs undergo progressive accumulation prior to EVs formation through membrane fusion-mediated release. Concomitantly, Immunohistochemistry (IHC) analysis demonstrated that MDBs formation spatially correlated with perisinusoidal macrophage infiltration, suggesting sterile inflammatory activation within this pathogenic cascade. (Fig. 7A). cGAS, a DNA sensor, detects mtDNA and activates downstream pathways that promote inflammatory processes. In our MDB-forming mouse model, both mRNA and protein levels of the cGAS-STING pathway were upregulated, with a notable increase in mRNA levels, although the protein level showed a weaker trend (Fig. 7B and Fig. S8). Concurrently, the mRNA level of IL-6, a common inflammatory factor, was also elevated (Fig. S9).

Moreover, cGAS-STING showed a tendency to be upregulated in isolated primary Kupffer cells (KCs) (Fig. 7C). IF analysis demonstrated increased co-localization of cGAS with mtDNA in the experimental group (Fig. 7D), accompanied by elevated STING expression (Fig. 7E), suggesting that mtDNA binds to intracellular DNA sensor cGAS in macrophages and activates STING. Flow cytometric result demonstrated enhanced IL-6 secretion in macrophages from DDC-treated mice relative to controls (Fig. 7F), with complementary ELISA quantification revealing marked elevation of IL-6 levels. (Fig. 7G). The release of IL-6 was further demonstrated by exposing immune cells, such as the RAW264.7 macrophage cell line, to isolated mitochondria [20]. As shown in Fig. 7H, mitochondria isolated from mice were added in specific proportions to RAW264.7 cells and cultured for 16 h. After culture, significant polarization of RAW264.7 cells was observed in the experimental group, and the mRNA level of IL-6 secretion was significantly increased (Fig. 7I–J). These results comprehensively illustrate how cGAS activates downstream pathways and releases IL-6, exacerbating the inflammatory environment following chronic liver injury.

Inhibition of JNK signaling reduces MDBs formation and alleviates inflammatory environment

JNK-IN-8 is a JNK pathway inhibitor that effectively suppresses the activation of the JNK pathway and its downstream effector, c-JUN [38]. To assess the impact of JNK signaling inhibition on MDBs formation, we pretreated MDB-forming Hepa1-6 cells, which were treated with TNF-α and IFN-γ, with exogenous JNK-IN-8. After 24 h of cultivation, JNK blockade significantly attenuated pathway activation, evidenced by reduced phospho-JNK and c-JUN levels, along with a reduction in UbD expression following inhibitor treatment (Fig. 8A and Fig. S10), suggesting that JNK pathway repression may inhibit MDBs formation.

IF staining further revealed decreased co-localization of K8 and p62 in MDB-forming Hepa1-6 cells after JNK inhibition (Fig. 8B). Additionally, JNK pathway inhibition stabilized mitochondrial membranes, effectively preventing the TOM20/mtDNA-containing MDVs formation (Fig. 8C). TEM revealed DMSO-treated cells displayed mitochondrial damage with autophagolysosomal activation, contrasting with JNK-inhibited counterparts maintaining organellar integrity (Fig. 8D), collectively delineating a mechanistic linkage between mitochondrial preservation and downstream sterile inflammation resolution.

(See figure on next page.)

Fig. 5 MDBs pathogenesis was associated with mitochondrial damage and MDVs formation. **A**, **B** TEM reveals mitochondrial and lysosomal morphology changes in control and experimental group. TEM shows single mitochondrial-derived vehicle (MDV) and aggregated MDVs at periphery of cell membrane. Bar = 500 nm or 100 nm. **C** Two destinations of MDVs were shown. **D** Liver lysates from DDC-treated and control group (n = 3 per group) were analyzed by western blot using the antibodies against TOM20. GAPDH served as a loading control. Bands were analyzed for grayscale values by ImageJ and quantified by using Prism software. **E** Cells was stimulated for 12, 24 and 48 h after TGF-β addition in vitro MDBs cell model. Then cellular proteins were collected and cell lysates were analyzed by Western blot using the antibodies against TOM20. β-actin served as a loading control. **F** IF analysis of morphological alterations of TOM20 with mtDNA in paraffin sections of mouse liver in control and experimental groups. Bar = 10 μm. **G** IF demonstrates morphological alterations of TOM20 with mtDNA in MDBs-like protein aggregate formation cell model in control and experimental groups. Bar = 100 μm. **H** Five randomly selected horizons were counted separately for the TOM20 binding mtDNA situation then statistically analyzed using Prism software

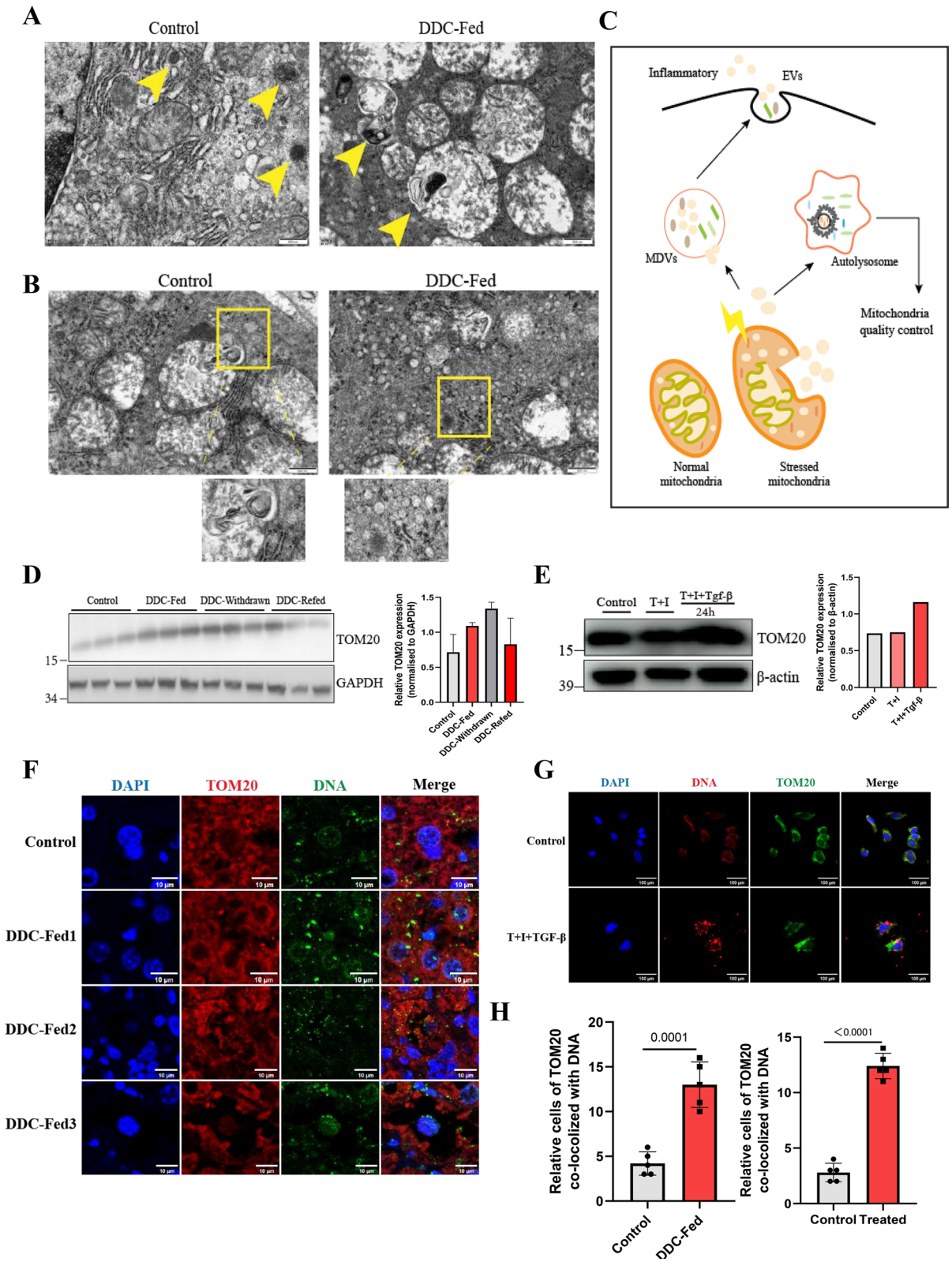

Fig. 5 (See legend on previous page.)

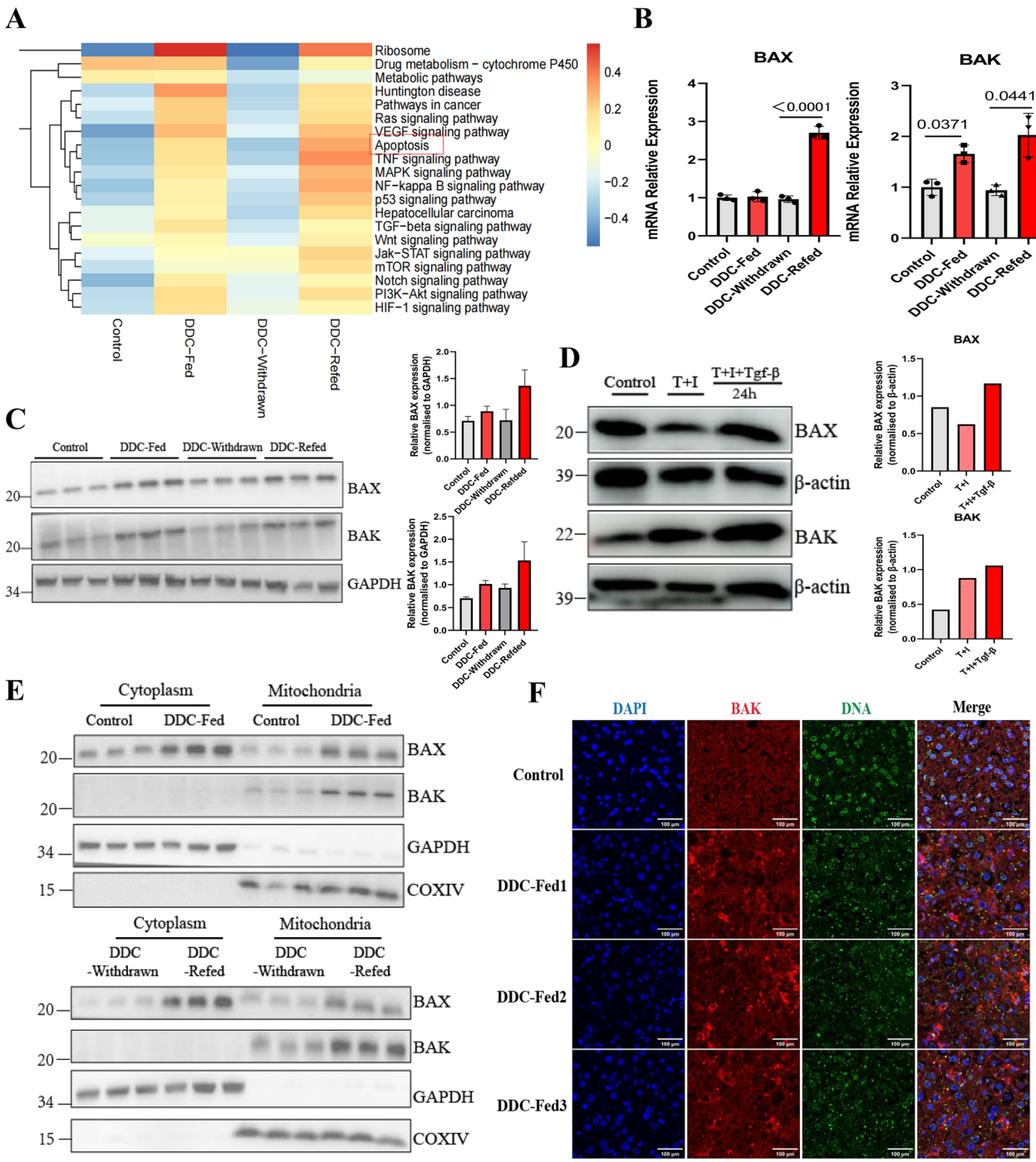

Fig. 6 TGF-β/JNK axis initiates downstream activation of apoptotic molecules. **A** GSVA analysis demonstrated multiple signaling pathways activated during MDBs pathological process. **B** Validation of BAX and BAK activation at mRNA level in MDBs mouse by RT-qPCR analysis. **C** Liver lysates of animal model 4 sets of samples (n = 3 per group) were analyzed by Western blot using the antibodies against BAX, BAK. GAPDH served as a loading control. Results shown are representative of three independent experiments. Bands were analyzed for grayscale values by ImageJ and quantified by using Prism software. **D** Cells was stimulated for 12, 24 and 48 h after TGF-β addition in vitro MDBs cell model. Then cellular proteins were collected and cell lysates were analyzed by Western blot using the antibodies against BAX and BAK. β-actin served as a loading control. **E** Isolation of cytoplasm and mitochondria from liver tissue of animal model (n = 3), then protein lysates were analyzed by Western blot using the antibodies against BAX and BAK. GAPDH served as a cytoplasmic loading control, COXIV served as a mitochondrial loading control. **F** IF demonstrates morphological alterations of BAK with mtDNA in paraffin sections of mouse liver in control and experimental groups. Bar = 100 μm

Interestingly, we found that the secretion of IL-6 was reduced in DDC-induced $UbD^{-/-}$ mice (Fig. 8E). To further validate whether JNK pathway inhibition affects inflammatory processes during MDBs pathogenesis, we established a transwell co-culture system with Hepa1-6 cells under varying JNK activation states and RAW264.7 macrophages. Following 24-h co-cultivation, macrophages were collected and subjected to intracellular cytokine staining for IL-6 quantification by flow cytometry. The results showed that RAW264.7 cells secreted more IL-6 when co-cultured with Hepa1-6 cells inducing MDBs formation. However, inhibition of JNK signaling significantly reversed this inflammatory secretion process (Fig. 8F-H). These findings suggest that inhibition of JNK pathway activation effectively mitigates MDBs formation and attenuates the inflammatory microenvironment.

Discussion

Extensive research has centered on delineating TGF-β-mediated epithelial-mesenchymal transition (EMT) and hepatic fibrosis through canonical SMAD-dependent signaling cascades [39, 40], evidence also demonstrates that the JNK pathway critically modulates hepatocyte dysfunction through orchestrating apoptosis, autophagy, and sustained inflammatory responses in diverse liver pathologies [41, 42]. Nevertheless, the crosstalk between TGF-β signaling and JNK-mediated regulatory networks under varying liver injury contexts remains underexplored. In this study, we mechanistically delineate the TGF-β/JNK axis as a pathogenic coordinator mediating MDBs formation with co-activation of pro-inflammatory signaling cascades. Our data demonstrate that TGF-β/JNK axis-mediated c-JUN activation mechanistically drives UbD promoter transactivation through direct DNA binding, as evidenced by dual-luciferase assays, thereby transcriptionally promoting MDBs formation. This regulatory axis was confirmed through UbD-/- mice, where UbD deficiency abrogated MDBs injury and induced concomitant c-JUN downregulation, validating their functional interdependence. Furthermore, we demonstrate that JNK-activated pro-apoptotic effectors BAX/BAK mediate mitochondrial permeabilization and leakage of fragmented mtDNA, which initiates MDVs formation and potentiates macrophage-driven inflammatory cascades.

While mitochondrial dysfunction has been epidemiologically associated with inflammatory cascades in chronic liver injury [43]. The precise mechanisms through which mitochondrial damage contributes to both MDBs formation and the establishment of inflammatory microenvironments remain to be elucidated. Accumulating evidence demonstrates that mtDNA can be released into the cytoplasm through mitochondrial BAX/BAK pores, VDAC pores, or the mitochondrial permeability transition pore [44–46]. Moreover, post-stress enrichment of TOM20 in the outer membrane confirms that mitochondrial outer membrane permeabilization facilitates mtDNA release into the cytoplasm [37]. Nevertheless, the detailed mechanism of mtDNA release during MDBs pathogenesis remains unknown. Additionally, mitochondria have evolved several quality control mechanisms to maintain their homeostasis in response to damage [47]. For example, the cytoplasmic ubiquitin–proteasome system and various mitochondrial chaperones regulate protein folding pathways, providing mitochondria with high plasticity to adapt to cellular needs [47, 48]. Our findings delineate a mitochondrial permeabilization cascade during chronic hepatic injury: Cytosolic BAX translocates to depolarized mitochondrial membranes, co-oligomerizing with resident BAK to form macromolecular pores facilitating the release of DAMPs. Crucially, mtDNA complexes with TOM20-positive outer membrane fragments, packaging into MDVs that extrude through BAX/BAK-formed macropores into the cytosol.

EVs have been conclusively demonstrated to mediate intercellular communication via trafficking of bioactive macromolecular cargo, exerting pleiotropic regulatory effects across diverse pathophysiological cascades [49–51]. Here, we postulate that damaged mitochondria

(See figure on next page.)

Fig. 7 mtDNA activates macrophage cGAS-STING signaling pathway to release IL-6. **A** IHC presents F4/80 staining in control and experimental groups, explaining the macrophage infiltration after DDC feeding. Meanwhile, 3 randomly selected visual field OD were counted and statistically analyzed. Bar = 100um. **B** Liver lysates from DDC-treated and control group (n = 3) were analyzed by Western blot using the antibodies against cGAS、STING、p-TBK1 and TBK1. GAPDH served as a loading control. **C** Isolation of primary KCs from MDBs livers (n = 3 per group), then protein lysates were analyzed by Western blot using the antibodies against cGAS、STING. β-actin served as a cytoplasmic loading control. **D**, **E** IF demonstrates mtDNA binding to DNA sensor cGAS and subsequent STING activation in primary macrophages. Bar = 50 μm or 10 μm. **F** The secretion of IL-6 of macrophages in mice was determined by flow cytometry. **G** Mice serum IL-6 expression level was validated by ELISA. **H** Schematic illustration of the quantification of inflammatory response experiment, isolated normal/damaged mitochondria were added to mouse macrophage cell line RAW264.7, and cellular RNA was extracted after 16 h of incubation, and the level of inflammatory factor IL-6 mRNA expression was detected by RT-qPCR assay. **I** Microscopic observation of cell morphology changes after normal/damaged mitochondria stimulation of RAW264.7 cells for 16 h. Bar = 20 μm. **J** IL-6 activation at mRNA level in quantification of inflammatory response was determined by RT-qPCR assay

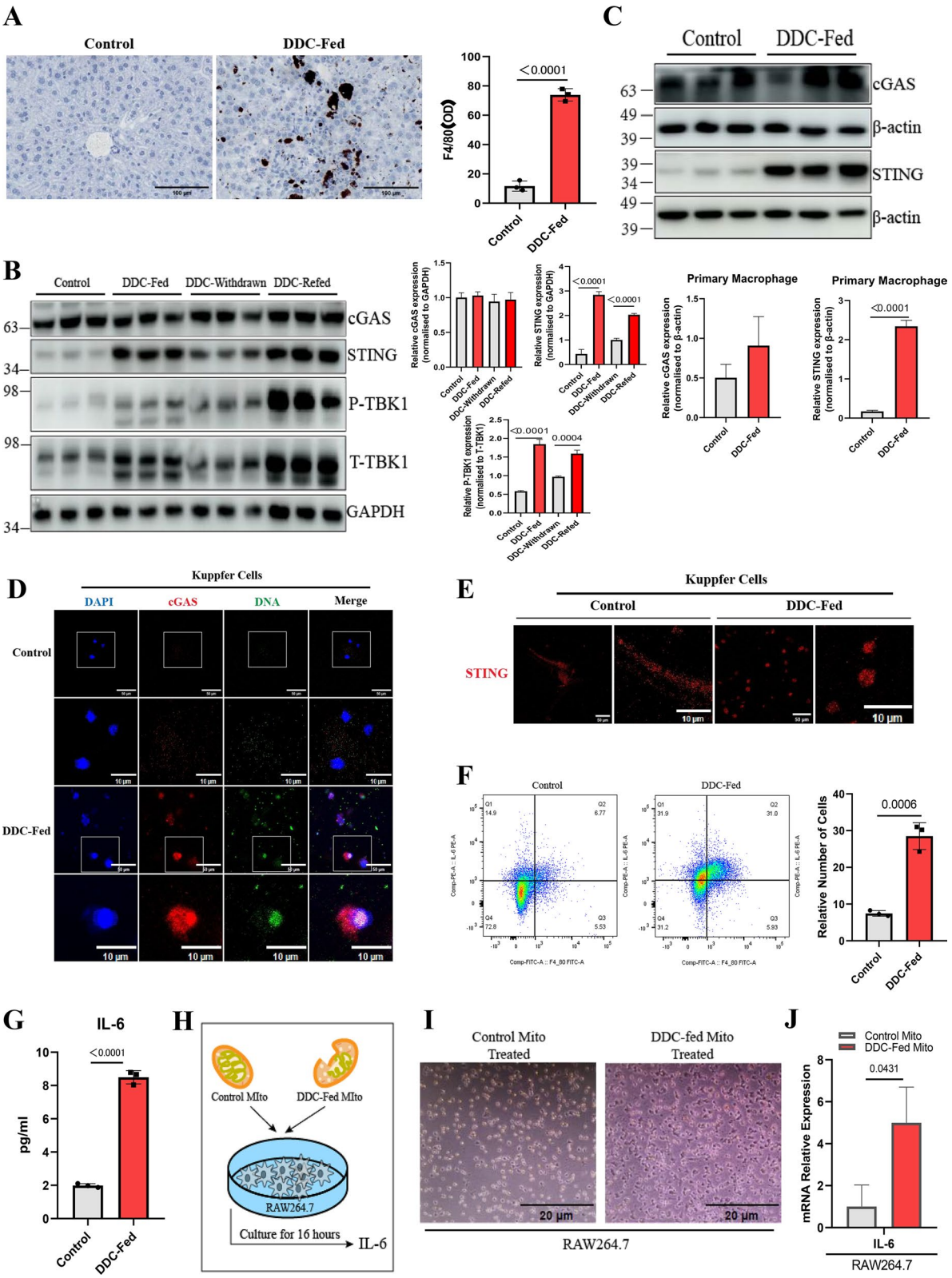

Fig. 7 (See legend on previous page.)

employ MDVs as vesicular carriers to facilitate lysosomal activation, with selective fusion generating autophagolysosomes that ensure mitochondrial quality control. Under overwhelming mitochondrial stress, pathological MDVs harboring cargo like mtDNA accumulate at organelle-membrane interfaces. These MDVs are subsequently packaged into EVs for intercellular transmission of mitochondrial danger signals. This process also allows cells to exchange proteins, lipids, and genetic material [52]. While understanding the heterogeneous membrane structure of cellular origin vehicles, such as EVs, is essential for elucidating their physiological and pathological functions, the origin, targeting, and fate of such extracellular vesicles remain topics of ongoing debate.

Emerging evidence indicates a significant association between chronic liver disease and concurrent mitochondrial dysfunction with macrophage infiltration. While Single-cell transcriptomic analysis has revealed signature pathogenic mechanisms of macrophage reprogramming within MDBs pathogenesis [53]. mtDNA and its receptor, cGAS, have become a focal point of research in recent years [54]. The cGAS-STING pathway has been shown to play a critical role in various pathological processes, including hepatocyte pyroptosis and autophagy [55, 56]. This suggests that the binding of endogenous DNA to cGAS is a key mechanism driving inflammation. IL-6, a common pro-inflammatory molecule, is activated in response to mtDNA stimulation through a cascade reaction. In this study, through immunofluorescence-based spatial colocalization analysis of primary Kupffer cell isolations, we demonstrated that cGAS activation is mediated by hepatocyte-derived mtDNA. We further conducted inflammation quantification experiments to confirm the morphological changes in the RAW264.7 cell line and the secretion of IL-6 following mitochondrial injury. Similarly, lower levels of IL-6 were detected in the serum of $UbD^{-/-}$ mice, suggesting that blocking MDBs formation attenuates the inflammatory response in vivo.

To conclude, our findings mechanistically delineate that TGF-β/JNK axis activation mediate MDVs release through BAX/BAK oligomerization pores during MDBs pathogenesis. These hepatocyte-derived MDVs activate macrophage cGAS-STING signaling via cytosolic mtDNA translocation, triggering IL-6-mediated pro-inflammatory cytokine secretion that sustains a self-perpetuating inflammatory cycle in vivo. Conventional antifibrotic therapeutics remain confined to monotherapeutic targeting of TGF-β pathways [57, 58], whereas our findings demonstrate that JNK inhibitors concomitantly attenuate pro-inflammatory microenvironment formation and suppress MDBs pathogenesis. This dual-pathway intervention establishes a novel therapeutic paradigm for the clinical management of MDB-associated chronic liver diseases (Fig. 8I).

Analysis of 16 clinical samples revealed a disruption in ubiquitin–proteasome function in MASLD patients, suggesting that the degradation of aberrantly aggregated proteins is impaired, accompanied by protein misfolding. Concurrently, the enrichment of neurological disease pathways, similar to MDBs formation, indicates the presence of MDBs in MASLD patients [59]. Moreover, through analysis of clinical hub genes and animal model sequencing data, we identified four key genes: SOD2, YARS, MARS, and FNDC4. YARS and MARS, as pro-oncogenic proteins, are implicated in the progression of several chronic diseases [33]. FNDC4, a hepatic secretory factor, is frequently associated with the accelerated formation of the inflammatory milieu in chronic liver diseases [60]. Additionally, SOD2 has been shown to play a critical role in various liver diseases via the TGF-β/JNK axis [15]. We further confirmed the correlation between SOD2 and the TGF-β/JNK axis through the Gene Ontology Database (https://geneontology.org/). Thus, identifying the TGF-β/JNK axis as a significant target in the pathogenesis of chronic liver diseases, including

(See figure on next page.)

Fig. 8 Inhibition of JNK pathway suppresses MDBs formation and alleviates inflammatory response. **A** In Hepa1-6 cell line, JNK activation was induced by stimulation with TGF-β (5 ng/ml) for 24 h on the basis of MDBs-like protein aggregate formation by TNF-α in combination with IFN-γ. The other groups were treated with JNK-IN-8 (3 μm) to inhibit the activation of the JNK pathway. Western blot was then used to verify the changes in expression of relevant proteins after JNK inhibition. β-actin served as a cytoplasmic loading control. **B** IF demonstrates K8 and p62 protein changes after DMSO and JNK-IN-8 treatment based on JNK pathway activation. ImageJ software was used to calculate fluorescence intensity of K8 and p62 in each group, and the co-localization of K8 and p62 was expressed as the ratio of the fluorescence intensity of K8 to that of p62. Then 3 randomly selected horizons were analyzed for fluorescence intensity and statistics. Bar = 100 μm. **C** IF demonstrates TOM20 binding mtDNA levels after DMSO and JNK-IN-8 treatment based on JNK pathway activation. TOM20-bingding mtDNA in each group was also counted and statistically analyzed in 5 randomly selected horizons. Bar = 100 μm. **D** The damage of cells, lysosomes and mitochondria in the control group, the TNF-α combined with IFN-γ and TGF-β stimulation group (treated with DMSO), and the TNF-α combined with IFN-γ and TGF-β stimulation group (treated with JNK-IN-8) was observed by TEM. Bar = 2 μm/500 μm. **E** $WT/UbD^{-/-}$ Mice serum IL-6 expression level was validated by ELISA. **F**–**H** Three groups of Hepa1-6 treated with different conditions were co-cultured with RAW264.7 for 24 h. RAW264.7 was collected and analyzed for secretion levels by flow cytometric counting after labeling with IL-6 (n = 3) and statistically analyzed. **H** Schematic illustration of proposed working model during liver MDBs formation in the present study

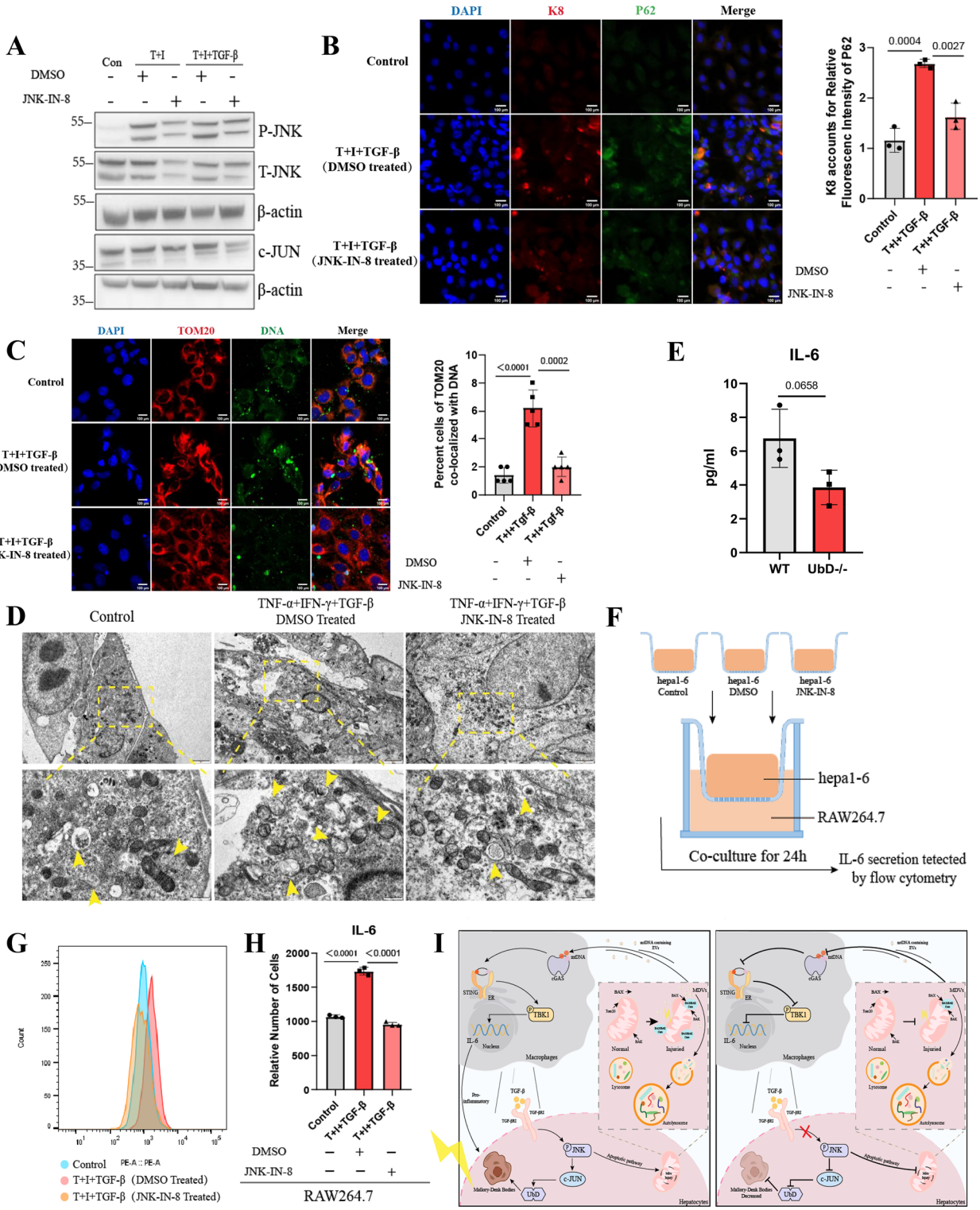

Fig. 8 (See legend on previous page.)

MDBs formation, is of great importance. The similarities observed between the pathological processes in clinical MASLD patients and our MDB-forming animal model suggest the potential for applying the therapeutic mechanisms identified in animal experiments to clinical settings.

Conclusions:

This study identifies the TGF-β/JNK axis as a crucial mechanism driving MDBs pathogenesis. We establish that MDVs mediate intercellular mtDNA transfer from injured hepatocytes to macrophages, triggering cGAS-STING-dependent IL-6 secretion and perpetuating inflammatory cascades. Moreover, WGCNA analysis of TGF-β/JNK axis activation in clinical MASLD patients, identifying the TGF-β/JNK axis as a significant target in the pathogenesis of MDB- related chronic liver diseases. Inhibiting this axis presents a therapeutic strategy to simultaneously suppress MDBs pathogenesis and sterile inflammation in chronic liver disorders.

Abbreviations

cGAS	Cyclic GMP-AMP synthase
cGAMP	2′,3′-Cyclic GMP-AMP
DDC	Diethyl 1, 4-dehydro-2, 4, 6-trimethyl-3, 5-pyridine-dicarboxylate
EVs	Extracellular vesicles
GSVA	Gene set variation analysis
FNDC4	Fibronectin Type III Domain Containing 4
HCC	Hepatocellular carcinoma
IL-6	Interleukin 6
IFN-γ	Interferon gamma
K8	Keratin 8
MDBs	Mallory-Denk bodies
MDVs	Mitochondrial-derived vesicles
mtDNA	Mitochondrial DNA
MOMP	Mitochondrial outer membrane permeabilization
MARS	Methionine tRNA ligase
MASLD	Metabolic dysfunction- associated steatotic liver disease
p62 (SQSTM1)	Sequestosome 1
ROS	Reactive oxygen species
snRNA-seq	Single-nucleus RNA sequencing
STING	Stimulator of interferon response CGAMP interactor
SOD2	Superoxide dismutase 2
TGF-β	Transforming growth factor beta
TNF-α	Tumor necrosis factor alpha
UbD	Ubiquitin D
WGCNA	Weighted correlation network analysis
YARS	Tyrosyl-tTRNA synthetase

Supplementary Information

The online version contains supplementary material available at https://doi.org/10.1186/s12967-025-06618-9.

Additional file 1: Fig. S1. Changes in the quantity of each cell subpopulation of MDBs forming mouse model induced by DDC

Additional file 2: Fig. S2. Levels of variation in the intensity of interactions among cell subpopulations of DDC- Withdrawn and Refed groups

Additional file 3: Fig. S3. SnRNA sequencing results analyzed with macrophages as ligand hepatocytes as receptor selection for ligand-receptor pairs expressed in control and DDC-Fed group of mouse model

Additional file 4: Fig. S4. GSVA analysis demonstrated signaling pathways activated during MDBs formation

Additional file 5: Fig. S5. In vitro modeling of cells in which combined TNF-α and IFN-γ stimulation induces the production of MDBs-like protein aggregates in Hepa1-6. Meanwhile, validation of the role of TGF-β in the formation of MDBs by additional addition of TGF-β

Additional file 6: Fig. S6, 7. Violin plots presenting the varying distribution levels of UbD, K8 and p62 among subpopulations in MDBs forming mouse model

Additional file 7

Additional file 8: Fig. S8. Simple schematic showing intracellular localization of BAX and BAK proteins and release of MDVs before and after mitochondrial injury

Additional file 9: Fig. S9. Validation of cGAS、STING、TBK1 and IL-6 activation at mRNA level in mouse model by RT-qPCR analysis

Additional file 10: Fig. S10. Western Blot was then used to verify the changes in expression of UbD after JNK inhibition. β-actin served as a cytoplasmic loading control

Additional file 11

Additional file 12

Additional file 13

Acknowledgements

We thank Guangzhou Genedenovo Biotechnology Co., Ltd. for their assistance with sequencing and bioinformatics analysis. We also acknowledge the members of the Samuel W. French laboratory at the Harbor-UCLA Medical Center for their technical assistance and valuable suggestions. English language editing was provided by Dr. Xingguang Luo from Yale University.

Author contributions

L.H., and T.X.P. designed and supervised the experiments, S.Y., and Z.W.M. analyzed and interpreted the data. L.H., and S.Y. wrote the manuscript. S.Y., and H.M.P. performed the cellular and most mouse experiments and prepared figures. Z.B. did the western blot analysis. Z.Y., and Z.J.Y did immunostaining analysis. T.X.P., and S.Y. did data analysis and all authors reviewed the manuscript.

Funding

This research was supported by the National Key Research and Development Program of China (No. 2022YFC2304800). It was also funded by the Guangzhou Key Laboratory of Biological Targeting Diagnosis, Therapy and Rehabilitation of Guangdong Higher Education Institutes (Grant No. 2021 KSYS009), and the Key-Area Research and Development Program of Guangdong Province (No. 2022B1111020002). Additional support was provided through the open research funds under Grant Number 202301–205 from the Affiliated Qingyuan Hospital of Guangzhou Medical University and Qingyuan People's Hospital, as well as the funds under Grant Number 2024SRP133 from the Fifth Affiliated Hospital of Guangzhou Medical University.

Availability of data and materials

The single-nucleus RNA sequencing (snRNA-seq) data generated in this study have been deposited in the GEO database under Accession number GSE201569. For details on GEO data linking and citation, please refer to: https://www.ncbi.nlm.nih.gov/geo/info/linking.html. Microarray datasets for NAFLD were obtained from the NCBI Gene Expression Omnibus (GEO) database (http://www.ncbi.nlm.nih.gov/geo/), with GSE260666 selected for analysis. These data are also available upon request from the corresponding author.

Declarations

Ethics approval and consent to participate

Formalin-fixed paraffin-embedded (FFPE) liver biopsies from patients with HCC (n = 10) were obtained from the archives of Qingyuan Affiliated Hospital of Guangzhou Medical University, following Institutional Review Board approval (IRB-2022–094). Cases with significant MDBs (n = 3) were selected and evaluated by experienced pathologists. The study adhered to the principles of the Declaration of Helsinki, with data analyzed anonymously. All procedures involving human sample collection were approved and registered at Medicalresearch.org.cn by the tissue bank of the Qingyuan Affiliated Hospital of Guangzhou Medical University (ChiCTR2400084248). Informed consent was obtained from all participants.

Animal experimental protocols were approved by the Animal Care Committee of Guangzhou Medical University (GY2022144 and GY2022-101).

Consent for publication
Informed consent was obtained from all participants. The study adhered to the principles of the Declaration of Helsinki, and all procedures involving human samples were approved and registered at Medicalresearch.org.cn by the tissue bank of the Qingyuan Affiliated Hospital of Guangzhou Medical University (ChiCTR2400084248). The work has not been published or is under consideration elsewhere. All the authors agree to submit the manuscript.

Competing interests
The authors declare that they have no competing interests.

Author details
[1]Precision Medicine Center, Department of Clinical Laboratory, The Fifth Affiliated Hospital of Guangzhou Medical University, Guangzhou, China. [2]The State Key Laboratory of Respiratory Disease and National Clinical Research Center for Respiratory Disease, Guangzhou 510530, China. [3]Department of Pathology, Harbor UCLA Medical Center, University of California, Torrance CA90502, USA. [4]Research Institute of Infectious Diseases, Guangzhou Eighth People's Hospital, Guangzhou Medical University, Guangzhou, China. [5]The Qingyuan Affiliated Hospital of Guangzhou Medical University, Qingyuan People's Hospital, Qingyuan, China.

Received: 1 March 2025 Accepted: 15 May 2025
Published online: 03 June 2025

References

1. Ali PI, Aboul-Enein H, Ghanem A. Enantioselective toxicity and carcinogenesis. Curr Pharm Anal. 2005;1:109–25.
2. Ganesan P, Kulik LM. Hepatocellular carcinoma: new developments. Clin Liver Dis. 2023;27(1):85–102.
3. Ali I, et al. Anticancer metallodrugs of glutamic acid sulphonamides: in silico, DNA binding, hemolysis and anticancer studies. RSC Adv. 2014;4(56):29629–41.
4. Ali I, et al. Glutamic acid and its derivatives: candidates for rational design of anticancer drugs. Fut Med Chem. 2013;5(8):961–78.
5. Ali I, et al. Synthesis and synergistic antifungal activities of a pyrazoline based ligand and its copper(II) and nickel(II) complexes with conventional antifungals. Microb Pathog. 2012;53(2):66–73.
6. Imran A, et al. Role of unani medicines in cancer control and management. Curr Drug Ther. 2019;14(2):92–113.
7. Ali I, et al. Progress in polymeric nano-medicines for theranostic cancer treatment. Polymers (Basel). 2020;12(3):598.
8. Kataura T, et al. A chemical genomics-aggrephagy integrated method studying functional analysis of autophagy inducers. Autophagy. 2021;17(8):1856–72.
9. Seki E, Brenner DA, Karin M. A liver full of JNK: signaling in regulation of cell function and disease pathogenesis, and clinical approaches. Gastroenterology. 2012;143(2):307–20.
10. Qian H, Ding WX. SQSTM1/p62 and hepatic Mallory-Denk body formation in alcohol-associated liver disease. Am J Pathol. 2023;193(10):1415–26.
11. Basaranoglu M, et al. Mallory-Denk bodies in chronic hepatitis. World J Gastroenterol. 2011;17(17):2172–7.
12. Principe DR, et al. TGF-β: duality of function between tumor prevention and carcinogenesis. J Natl Cancer Inst. 2014;106(2):djt369.
13. Trelford CB, Dagnino L, Di Guglielmo GM. Transforming growth factor-β in tumour development. Front Mol Biosci. 2022;9: 991612.
14. Fang JY, Richardson BC. The MAPK signalling pathways and colorectal cancer. Lancet Oncol. 2005;6(5):322–7.
15. Rossi C, et al. Role of TGF-β1/miR-382-5p/SOD2 axis in the induction of oxidative stress in CD34+ cells from primary myelofibrosis. Mol Oncol. 2018;12(12):2102–23.
16. Zorov DB, Juhaszova M, Sollott SJ. Mitochondrial reactive oxygen species (ROS) and ROS-induced ROS release. Physiol Rev. 2014;94(3):909–50.
17. Fromenty B, Roden M. Mitochondrial alterations in fatty liver diseases. J Hepatol. 2023;78(2):415–29.
18. Longo M, et al. Mitochondrial dynamics and nonalcoholic fatty liver disease (NAFLD): new perspectives for a fairy-tale ending? Metabolism. 2021;117: 154708.
19. Sugiura A, et al. A new pathway for mitochondrial quality control: mitochondrial-derived vesicles. Embo j. 2014;33(19):2142–56.
20. Todkar K, et al. Selective packaging of mitochondrial proteins into extracellular vesicles prevents the release of mitochondrial DAMPs. Nat Commun. 2021;12(1):1971.
21. König T, McBride HM. Mitochondrial-derived vesicles in metabolism, disease, and aging. Cell Metab. 2024;36(1):21–35.
22. Decout A, et al. The cGAS-STING pathway as a therapeutic target in inflammatory diseases. Nat Rev Immunol. 2021;21(9):548–69.
23. Oduro PK, et al. The cGAS-STING signaling in cardiovascular and metabolic diseases: future novel target option for pharmacotherapy. Acta Pharm Sin B. 2022;12(1):50–75.
24. Li J, et al. S-adenosylmethionine prevents Mallory Denk body formation in drug-primed mice by inhibiting the epigenetic memory. Hepatology. 2008;47(2):613–24.
25. Ma Y, Zhang L, Huang X. Genome modification by CRISPR/Cas9. Febs j. 2014;281(23):5186–93.
26. Oliva J, et al. The role of cytokines in UbD promoter regulation and Mallory-Denk body-like aggresomes. Exp Mol Pathol. 2010;89(1):1–8.
27. Wang Z, et al. Identification of driver genes in lupus nephritis based on comprehensive bioinformatics and machine learning. Front Immunol. 2023;14:1288699.
28. Zhang YE. Non-Smad pathways in TGF-beta signaling. Cell Res. 2009;19(1):128–39.
29. Deng Z, et al. TGF-β signaling in health, disease, and therapeutics. Signal Transduct Target Ther. 2024;9(1):61.
30. Mark ZA, et al. Tobacco smoke condensate induces morphologic changes in human papillomavirus-positive cervical epithelial cells consistent with epithelial to mesenchymal transition (EMT) with activation of receptor tyrosine kinases and regulation of TGFB. Int J Mol Sci. 2024;25(9):4902.
31. Harada M, et al. Autophagy activation by rapamycin eliminates mouse Mallory-Denk bodies and blocks their proteasome inhibitor-mediated formation. Hepatology. 2008;47(6):2026–35.
32. Sorrentino V, Menzies KJ, Auwerx J. Repairing mitochondrial dysfunction in disease. Annu Rev Pharmacol Toxicol. 2018;58:353–89.
33. Jordanova A, et al. Disrupted function and axonal distribution of mutant tyrosyl-tRNA synthetase in dominant intermediate Charcot-Marie-Tooth neuropathy. Nat Genet. 2006;38(2):197–202.
34. Nanayakkara R, et al. Autophagic lysosome reformation in health and disease. Autophagy. 2023;19(5):1378–95.
35. Chen F. JNK-induced apoptosis, compensatory growth, and cancer stem cells. Cancer Res. 2012;72(2):379–86.
36. Sui X, et al. p38 and JNK MAPK pathways control the balance of apoptosis and autophagy in response to chemotherapeutic agents. Cancer Lett. 2014;344(2):174–9.
37. Bock FJ, Tait SWG. Mitochondria as multifaceted regulators of cell death. Nat Rev Mol Cell Biol. 2020;21(2):85–100.
38. Li R, et al. Therapeutically reprogrammed nutrient signalling enhances nanoparticulate albumin bound drug uptake and efficacy in KRAS-mutant cancer. Nat Nanotechnol. 2021;16(7):830–9.
39. Geng XQ, et al. Ganoderic acid hinders renal fibrosis via suppressing the TGF-β/Smad and MAPK signaling pathways. Acta Pharmacol Sin. 2020;41(5):670–7.
40. Zhang K, et al. Targeting GPR65 alleviates hepatic inflammation and fibrosis by suppressing the JNK and NF-κB pathways. Mil Med Res. 2023;10(1):56.
41. Malhi H, Kaufman RJ. Endoplasmic reticulum stress in liver disease. J Hepatol. 2011;54(4):795–809.
42. Yang YM, Kim SY, Seki E. Inflammation and liver cancer: molecular mechanisms and therapeutic targets. Semin Liver Dis. 2019;39(1):26–42.
43. Brenner C, et al. Decoding cell death signals in liver inflammation. J Hepatol. 2013;59(3):583–94.
44. McArthur K, et al. BAK/BAX macropores facilitate mitochondrial herniation and mtDNA efflux during apoptosis. Science. 2018;359(6378):aao6047.
45. Kim J, et al. VDAC oligomers form mitochondrial pores to release mtDNA fragments and promote lupus-like disease. Science. 2019;366(6472):1531–6.
46. Yu CH, et al. TDP-43 triggers mitochondrial DNA release via mPTP to activate cGAS/STING in ALS. Cell. 2020;183(3):636-649.e18.

47. Ng MYW, Wai T, Simonsen A. Quality control of the mitochondrion. Dev Cell. 2021;56(7):881–905.
48. Borcherding N, Brestoff JR. The power and potential of mitochondria transfer. Nature. 2023;623(7986):283–91.
49. Peruzzotti-Jametti L, et al. Neural stem cells traffic functional mitochondria via extracellular vesicles. PLoS Biol. 2021;19(4): e3001166.
50. Couch Y, et al. A brief history of nearly EV-erything—the rise and rise of extracellular vesicles. J Extracell Vesicles. 2021;10(14): e12144.
51. Kalluri R. The biology and function of extracellular vesicles in immune response and immunity. Immunity. 2024;57(8):1752–68.
52. van Niel G, D'Angelo G, Raposo G. Shedding light on the cell biology of extracellular vesicles. Nat Rev Mol Cell Biol. 2018;19(4):213–28.
53. Fang Z, et al. Single-cell transcriptomic analysis reveals characteristic feature of macrophage reprogramming in liver Mallory-Denk bodies pathogenesis. J Transl Med. 2025;23(1):77.
54. Motwani M, Pesiridis S, Fitzgerald KA. DNA sensing by the cGAS-STING pathway in health and disease. Nat Rev Genet. 2019;20(11):657–74.
55. Liu Z, et al. XBP1 deficiency promotes hepatocyte pyroptosis by impairing mitophagy to activate mtDNA-cGAS-STING signaling in macrophages during acute liver injury. Redox Biol. 2022;52: 102305.
56. Li Y, et al. Increased Drp1 promotes autophagy and ESCC progression by mtDNA stress mediated cGAS-STING pathway. J Exp Clin Cancer Res. 2022;41(1):76.
57. Ong CH, et al. TGF-β-induced fibrosis: a review on the underlying mechanism and potential therapeutic strategies. Eur J Pharmacol. 2021;911: 174510.
58. Peng H, et al. Local release of TGF-β inhibitor modulates tumor-associated neutrophils and enhances pancreatic cancer response to combined irreversible electroporation and immunotherapy. Adv Sci (Weinh). 2022;9(10): e2105240.
59. French SW, Mendoza AS, Peng Y. The mechanisms of Mallory-Denk body formation are similar to the formation of aggresomes in Alzheimer's disease and other neurodegenerative disorders. Exp Mol Pathol. 2016;100(3):426–33.
60. Bosma M, et al. FNDC4 acts as an anti-inflammatory factor on macrophages and improves colitis in mice. Nat Commun. 2016;7:11314.

Publisher's Note